

Contact Resistance Optimization in MoS₂ Field-Effect Transistors through Reverse Sputtering-Induced Structural Modifications

Yuan Fa^{1,2}, Agata Piacentini^{1,2}, Bart Macco³, Holger Kalisch⁴, Michael Heuken^{4,5}, Andrei Vescan⁴, Zhenxing Wang^{1,*}, and Max C. Lemme^{1,2,*}

¹ AMO GmbH, Advanced Microelectronic Center Aachen, Otto-Blumenthal-Str. 25, 52074 Aachen, Germany

² Chair of Electronic Devices, RWTH Aachen University, Otto-Blumenthal-Str. 25, 52074 Aachen, Germany

³ Department of Applied Physics and Science Education, Eindhoven University of Technology, 5600 MB Eindhoven, The Netherlands

⁴ Compound Semiconductor Technology, RWTH Aachen University, 52074 Aachen, Germany

⁵ AIXTRON SE, 52134 Herzogenrath, Germany

Abstract

Two-dimensional material (2DM)-based field-effect transistors (FETs), such as molybdenum disulfide (MoS₂)-FETs, have gained significant attention for their potential for ultra-short channels, thereby extending Moore's law. However, MoS₂-FETs are prone to the formation of Schottky barriers at the metal-MoS₂ interface, resulting in high contact resistance (R_c) and, consequently, reduced transistor currents in the ON-state. Our study explores the modification of MoS₂ to induce

the formation of conductive 1T-MoS₂ at the metal-MoS₂ interface via reverse sputtering. MoS₂-FETs exposed to optimized reverse sputtering conditions in the contact area show R_c values reduced to less than 50% of their untreated counterparts. This reduction translates into improvements in other electrical characteristics, such as higher ON-state currents. Since reverse sputtering is a standard semiconductor process that enhances the electrical performance of MoS₂-FETs, it has great potential for broader application scenarios in 2DM-based microelectronic devices and circuits.

Introduction

Silicon-based field-effect transistors (FETs), the fundamental components of integrated circuits, are approaching their physical limits at physical gate lengths of approximately 10 nm.¹ New materials may be capable of overcoming these constraints, thus enabling the continuation of miniaturizing integrated circuits. Molybdenum disulfide (MoS₂), a semiconducting two-dimensional (2D) transition metal dichalcogenide (TMDC), has emerged as a promising channel material because of its potential for next-generation FETs.²⁻¹¹ Its ultra-thin structure enables ideal electrostatic control of the channel potential by the gate electrode, facilitating low OFF-currents (I_{off}). In addition, high ON-currents (I_{on}) are achievable through multiple-channel stacking.^{12,13} Additionally, in contrast to silicon, the layered nature of MoS₂ enables it to maintain excellent carrier mobility down to the monolayer regime.^{11,14,15}

MoS₂ is a polymorphic material and exists in different structural forms, with the most common being the trigonal prismatic coordination (2H) and octahedral symmetry (1T) phases. The 2H phase, which is thermodynamically stable and commonly found in natural MoS₂ crystals, is semiconducting. Bulk 2H-MoS₂ is a semiconductor with an indirect bandgap of 1.2 eV, which transitions to a direct bandgap of 1.8 eV for monolayer MoS₂.¹⁶ Conversely, the 1T phase of MoS₂ is metallic, with a conductivity 10⁷ times greater than that of the 2H phase.^{17,18} It is metastable and can be chemically synthesized. In addition, the transition from the 2H to 1T phase can be achieved by shifting a sulfur atom within the unit cell from one pyramidal position to another.¹⁹

MoS₂ has become an attractive candidate among TMDs for advanced transistor applications due to its tunable band gap and polymorphism, moderately high carrier mobility³ even at the monolayer

limit, and mechanical flexibility.²⁰ MoS₂-FETs have been proposed for analog and digital electronics because of their large on/off-current ratios of up to 10¹⁰, mobility of approximately 200 cm²·V⁻¹·s⁻¹, and a subthreshold swing approaching the theoretical limit of 60 mV/dec at room temperature.⁹ Despite these excellent properties, achieving low contact resistances (R_c) remains challenging because a Schottky barrier forms at the MoS₂-metal interface. Unlike conventional transistors, where low R_c can be achieved by high (degenerate) doping of the semiconductor, this approach is not applicable in MoS₂-based FETs. The large Schottky barrier height (SBH) restricts electron injection and degrades performance.^{21,22}

Several approaches have been devoted to lowering the SBH and reducing R_c in MoS₂-FETs. Promisingly, zero SBH and ohmic contacts to monolayer TMDCs have been achieved with the semimetals bismuth (Bi) and antimony (Sb),^{23–25} although their low abundance may pose challenges for sustainable large-scale production. Contact deposition under ultrahigh vacuum (UHV) conditions has also been shown to reduce R_c to MoS₂-FETs, even with complementary metal oxide semiconductor (CMOS) technology-compatible metals.²⁶ However, UHV deposition may not be cost-efficient for mass production. Recently, low R_c was achieved using heterostructures of semimetallic (CVD-grown) monolayer graphene and MoS₂.^{6,27} However, fabricating 2D heterostructures increases the complexity of this approach. Kappera *et al.* presented a chemical method to induce a MoS₂ phase transition to design heavily doped source and drain contacts to achieve a low R_c .⁴ However, this method has limitations due to the chemical toxicity involved, and it has not yet been demonstrated on polycrystalline CVD materials required for wafer-scale integrated circuits. Furthermore, MoS₂-FETs have been exposed to argon (Ar) plasma

to reduce R_c by either inducing a phase transition to 1T-MoS₂ at the metal contact interface⁷ or by creating sulfur vacancies (V_s)⁸, although more detailed studies are required to understand the relationship between the phase transition and defect concentration in MoS₂.

Reverse sputtering employs Ar ions produced by radio frequency (RF) generated plasma, which are attracted to the substrate by a negative bias in a vacuum chamber. This method is attractive because of its cleanliness, scalability, and controllability, and it can be combined *in situ* with metal sputter deposition, enabling a controlled contact fabrication process. Here, we demonstrate a scalable methodology to reduce R_c in metal-organic chemical-vapor-deposited (MOCVD) MoS₂-based FETs through reverse sputtering. We analyzed MoS₂ with photoluminescence (PL) and Raman spectroscopy to verify the influence of reverse sputtering at process parameters and conducted X-ray photoelectron spectroscopy (XPS), which indicated the existence of 1T phase MoS₂ and S vacancies in the sputter-treated material. We fabricated MoS₂-FETs with nickel (Ni) top-contacts (TOP-FETs) to the sputter-induced 1T-MoS₂ and pristine 2H-MoS₂ as the channel, and control FETs with bottom-contacts (BOT-FETs) where the entire MoS₂, i.e. channel and electrode regions, was exposed to the Ar plasma. While the former devices showed improved R_c , the latter lost gate modulation. This demonstrates the feasibility of our approach toward scalable contact engineering in MoS₂-FETs.

Results and Discussion

All experiments were carried out on silicon (Si) chips ($2 \times 2 \text{ cm}^2$) covered with 90 nm thermal SiO₂. The MoS₂ material was grown via metal-organic chemical vapor deposition (MOCVD) on

sapphire substrates. Details of the material growth and device fabrication are described in the Methods section.

Atomic force microscopy (AFM) was conducted to measure the layer thickness of the pristine MOCVD MoS₂ on the as-grown sapphire wafer (Fig. 1a). The inset height profile shows a MoS₂ film height of 2.5 nm, corresponding to approximately four layers if we assume a thickness of monolayer MoS₂ of 0.65 nm.²⁸

We then prepared four SiO₂/Si substrates with MoS₂ transferred onto them. One sample was kept in its pristine state without any treatment, whereas the other three samples were subjected to reverse sputtering at different power levels of 25 W, 75 W, and 200 W for 10 s. Afterwards, PL and Raman spectroscopy were conducted. Fig. 1b shows the PL spectra of pristine MoS₂ and the sputter-treated MoS₂ films. A distinct peak is observed at approximately 1.80 eV in the PL of pristine MoS₂, corresponding to the characteristic A exciton and indicating its semiconductor properties.²⁹ Sputter treatments with 25 W, 75 W, and 200 W resulted in PL quenching, which was stronger for increasing power. The PL quenching can be attributed to an increasing vacancy or defect concentration and a transition from a semiconducting state to a metallic state, namely, the 2H to 1T transition (see also XPS data below).^{7,30,31} We also noticed a shift toward higher PL photon energy upon sputter exposure. The PL spectra obtained at 25 W were also gradually quenched as the duration increased (see supporting information (SI) Fig. S1).

Following this initial experiment, the three sputter-treated samples underwent additional 10-second increments of sputter exposure with the same power until a total duration of 50 s was reached. We again used Raman spectroscopy to investigate the MoS₂. Fig. 1c-e show the average Raman spectra

of the MoS₂ in an area of 5 μm × 5 μm obtained at the different sputtering power levels (see details in the Methods section). Each graph shows the spectra taken after 10, 20, 30, 40, and 50 s of sputter exposure and includes a Raman spectrum of pristine MoS₂ for reference (purple). The distinct peaks corresponding to the in-plane (E_{2g}¹) and out-of-plane (A_{1g}) modes are observed at approximately 382.0 cm⁻¹ and 406.7 cm⁻¹, with a position difference Δ of 24.7 cm⁻¹. Additionally, a small new peak labeled **J** emerges at ~277 cm⁻¹ (more details of the intensity of the **J** peak in SI Fig. S2a), suggesting the creation of a distorted structure that includes a 2a₀ × a₀ basal plane superlattice and distorted octahedral coordination in the MoS₂ crystalline structure.³² The Raman spectrum of the sample at 25 W for 10 s in Fig. 1c shows increased intensities of the E_{2g}¹ and A_{1g} peaks, possibly due to alterations in the electronic band structure enhancing the interaction between electrons and A_{1g} phonons.³³ Combined with the PL data of 25 W for 10 s, this suggests a different crystalline structure in MoS₂ compared with pristine MoS₂ and other reverse sputtering parameters. In addition, the E_{2g}¹ and A_{1g} peaks in Fig. 1d-e exhibit a notable redshift, which becomes more pronounced with increasing sputtering duration, with a maximum value of approximately 2 cm⁻¹. This indicates weakened in-plane and out-of-plane vibrations of the Mo-S bonds and is a typical signal of a reduced layer number of MoS₂,^{34,35} meaning that the overall thickness of the multilayer MoS₂ in the 5 μm × 5 μm area was slightly reduced by reverse sputtering. Moreover, as the treatment duration and sputtering power increase, the E_{2g}¹, A_{1g}, and **J** peaks exhibit broadening and intensity degradation (more details in SI Fig. S2), culminating in a flat spectrum for the case of 200 W for 50 s in Fig. 1e. This indicates a progressive loss of MoS₂ crystalline structure, the emergence of Vs, structural disruption, and the potential presence of MoO_x.^{36,37}

XPS was used to evaluate the effects of reverse sputtering on the stoichiometry and binding configuration. It was performed on the pristine multilayer MoS₂ sample and the three samples exposed to 10 s of reverse sputtering with 25, 75, and 200 W of power. The pristine MoS₂ sample has an S/Mo ratio close to 2 (Fig. 2a). Reverse sputtering leads to a reduced stoichiometry, with the S/Mo ratio of the 200 W sample decreasing to 1.80, which could be a result of a large number of V_S in the crystalline structure of MoS₂. Fig. 2b-c show the Mo3d and S2p spectra, respectively. For pristine MoS₂, the binding energies of Mo3d_{5/2} and Mo3d_{3/2} are 230.1 eV and 233.2 eV, and the binding energies of S2p_{3/2} and S2p_{1/2} are 162.9 eV and 164.1 eV, respectively. Qualitatively, reverse sputtering induces broadening of the Mo3d, S2s, and S2p peaks as well as a shift to lower binding energies. The broadening is a sign of increased disorder in the system, whereas the binding energy shift is thought to originate from the 2H to 1T phase transition, both induced by Ar⁺ ion bombardment, in line with the literature.^{7,8} To quantify the phases, the Mo3d⁴⁺ peak was fitted with two contributions. The 1T contribution was constrained to have a binding energy 0.9 eV higher than the 2H phase contribution.³⁸ The pristine sample predominantly displays a semiconducting 2H phase, with a minor fitted metallic 1T phase. Moreover, the accurate quantification of oxygen in the MoS₂ layers is hindered because the MoS₂ layers are placed directly on a 90 nm SiO₂ film. However, we observed an additional weak peak at approximately 236 eV in the XPS spectrum of the 200 W 10 s sample, corresponding to the higher oxidation state of Mo⁺⁶.³⁹ An increase in the O1s contribution at approximately 531 eV is observed after reverse sputtering (Fig. 2d), which indicates enhanced oxidation of the MoS₂ layers in the ambient environment after reverse sputtering and a stronger binding effect of Mo-O.⁴⁰ While pristine MoS₂ is relatively resilient to

oxidation, reverse sputtering effectively creates V_s , which, upon ambient exposure, can be more easily oxidized to MoO_x . After all the sputter treatments, only a metallic 1T phase is obtained from the fitting procedure in Fig. 2b, implying full-phase conversion. As the 2H to 1T phase transition can be driven by V_s ,^{5,7} this is also in line with the reduced S/Mo ratio, as shown in Fig. 2a. While XPS suggests that 10 s of reverse sputtering at 25 W is sufficient to complete the 2H to 1T phase transition, higher sputtering powers result in additional modification of MoS_2 : the S/Mo ratio decreases, additional broadening of the S2p peak is observed, and an additional O1s contribution appears. Hence, there seems to be a balance between phase conversion and excessive damage to MoS_2 via reverse sputtering.

After the basic material characterization, we investigated the influence of reverse sputtering on the performance of MoS_2 -FETs with a channel width (W) of 25 μm . We conducted electrical measurements on 4 different samples of TOP-FETs in a vacuum: a pristine sample and three sputter-treated samples treated with 25 W, 75 W, and 200 W for a fixed duration of 10 s; the same parameters used for the XPS analysis. Notably, the channel MoS_2 remained in a pristine state in the top-contact configuration as it was protected by a photoresist during the optical lithography process (see Methods), while the MoS_2 under the source and drain metal was subjected to reverse sputtering as shown in the schematic and the microscope image in Fig. 3a). More details on the fabrication process are provided in the Methods section and SI Fig. S3. In Fig. 3b, the output characteristics of four TOP-FETs with a channel length (L_{ch}) of 4 μm are presented for each sample. Most evidently, the output current (I_{out}) of the device subjected to 75 W reverse sputtering is significantly greater by approximately 150 times than that of the pristine TOP-FET, whereas I_{out}

returns to the level of the pristine TOP-FET when exposed to 200 W reverse sputtering. Fig. 3c shows the statistical distribution of the two-probe FET mobility (μ_{2p}) for seven FETs with increasing L_{ch} on each sample, which was calculated via equations 1 and 2 from 2-terminal measurements:

$$\mu_{2p} = \frac{L_{ch}}{WC_iV_{SD}} \left(\frac{\partial I_D}{\partial V_{GS}} \right) \quad (1)$$

$$C_i = \frac{\epsilon_{SiO_2}\epsilon_0}{t_{ox}} \quad (2)$$

C_i represents the gate-channel capacitance per unit area. ϵ_{SiO_2} represents the relative permittivity of silicon dioxide, equal to 3.9. $\epsilon_0 = 8.854 \times 10^{-12} \text{ F}\cdot\text{m}^{-1}$ represents the vacuum permittivity, and t_{ox} represents the oxide thickness. In our case, L_{ch} ranges from 4 to 10 μm , W equals 25 μm , and t_{ox} is 90 nm. μ_{2p} is derived from two-probe measurements, which include a voltage drop across the Schottky barrier between 2D MoS₂ and metal contacts.⁴¹ Therefore, μ_{2p} serves as an indicator of the contact performance of the TOP-FETs, provided that the channel material is of the same quality. By fitting a Gaussian distribution to the histogram data, the mean value and standard deviation of μ_{2p} for each sample are as follows: 0.48 ± 0.10 , 0.52 ± 0.11 , 0.81 ± 0.20 , and $0.17 \pm 0.06 \text{ cm}^2\cdot\text{V}^{-1}\cdot\text{s}^{-1}$ for the pristine sample, 25 W, 75 W, and 200 W treatments, respectively. An increase in μ_{2p} for the 75 W sample is observed, nearly doubling compared with that of the pristine sample. While the 25 W sample shows barely any increase in μ_{2p} , the 200 W sample exhibits degradation. Fig. 3d-g show n-type transfer characteristics of seven TOP-FETs with increasing (L_{ch}) for a V_{DS} of 1 V for pristine and different treatment powers. The TOP-FETs on the pristine, 25 W, and 75 W samples (Fig. 3d-f) exhibit on/off current ratios of 10^6 , and the transfer curves on a linear scale

clearly reveal an increase in the I_{on} with increasing power. However, the on/off ratio of the 200 W sample degrades to 10^5 , and a decrease in I_{on} can also be observed. These transfer characteristics are compatible with the output characteristics described in Fig. 3b.

Fig. 4a-d displays the Transfer Length Method (TLM) plots for 28 TOP-FETs in 4 groups with L_{ch} ranging from 4 to 10 μm on each sample under an overdrive voltage (V_{ov}) of 19 V at a carrier concentration (n_s) of approximately $4.3 \times 10^{12} \text{ cm}^{-2}$. Table 1 presents the corresponding average values of R_c and the sheet resistance (R_{sh}) as well as their standard deviations extracted from TLM. The R_c of the sample subjected to 75 W decreased to 413 $\text{k}\Omega \cdot \mu\text{m}$ from 1126 $\text{k}\Omega \cdot \mu\text{m}$ for the pristine sample. The underlying reason for the improved contact performance lies in two factors. On the one hand, V_s introduced by reverse sputtering can create highly n-type doped regions in MoS_2 crystalline structures. This doping narrows the Schottky barrier, enabling electrons to tunnel through it more easily, thereby reducing R_c .⁸ On the other hand, V_s promote the phase transition from 2H to 1T, which is structurally achieved by transverse displacement of the S planes. In this case, conductive 1T- MoS_2 forms more easily, enhancing the injection of electrons from the Ni into the metallic 1T phase and then from the 1T into the 2T phase.^{17,19} Furthermore, the R_c of the 25 W sample increases by approximately 50% compared with that of the pristine sample. The reason may be that the reverse sputtering does not create a sufficient number of V_s with this parameter. In addition, the R_c of the 200 W sample is significantly higher than that of the other samples, which can likely be attributed to substantial oxidation to MoO_x caused by a large number of V_s , as supported by the XPS results. The presence of MoO_x in the MoS_2 structure distorts the crystalline structure of MoS_2 , which reduces the conductivity of the 2D material under the contact metal and

degrades the electrical performance of the TOP-FETs.⁴² The R_{sh} values of the reference sample and the 25 W and 75 W samples remained at the same resistive level, indicating that the pristine channel MoS₂ was unaffected by reverse sputtering. However, the R_{sh} of the 200 W sample was exceptionally high. We attribute this to excessive damage to the MoS₂ channel during the high-power sputtering process and the subsequent exposure of the highly defective MoS₂ channel to the ambient environment, which resulted in the formation of highly resistive MoOx. We also fabricated bottom-contact BOT-FETs as a control experiment, where we deposited the source and drain contacts before transferring the MoS₂ films (more details of the device fabrication are provided in the Methods section and SI Figs. S4 and S5a). Here, we exposed the entire MoS₂ in the channel and contact areas to the sputter treatment. Electrical measurements conducted in ambient air conditions showed that the total resistance (R_{tot}) decreased by several orders of magnitude upon high-power sputtering (SI Fig. S5b). However, apart from the case of 25 W for 10 s, where weak gate control is still observed, the transfer curves of BOT-FETs under 75 W and 200 W exhibit a complete loss of gate control. Additionally, the drain current (I_D) increases by more than five orders of magnitude compared to the I_{off} of the pristine BOT-FET (SI Fig. S5c-e). These combined results collectively confirm a transition of the MoS₂ to the metallic phase.

Conclusion

We investigated the potential of reverse sputtering for reducing the contact resistance to FETs with 2D MoS₂ channel. We show that the Ar⁺ bombardment in a reverse sputter process modifies the crystalline structure of multilayer MOCVD MoS₂ from pristine 2H-MoS₂ to metallic 1T-MoS₂

through PL, Raman, and X-Ray photoelectron spectroscopy. We demonstrated the method by evaluating the electrical performance of MoS₂-FETs and showed the effects of varying the sputtering power and duration. We found an optimum within our experimental split for a reverse sputtering power of 75 W for 10 s, as these devices exhibited a 50% reduction in R_c compared to untreated reference devices. The reduced R_c improved electrical performance metrics such as I_{on} , I_{out} , and mobility μ_{2p} . The results can be explained by the introduction of sulfur vacancies by the sputtering process, which facilitates the phase transition from 2H- to 1T-MoS₂ and narrows the Schottky barrier width to the Ni contact metal. However, R_c reduction was not achieved with inappropriate sputtering power, whether too weak (25 W) or too strong (200 W). Our findings suggest reverse sputtering as a highly efficient, large-scale, and CMOS-compatible method to optimize R_c in MoS₂-FETs.

Methods

Device fabrication: Si chips ($2 \times 2 \text{ cm}^2$) covered with 90 nm thermal SiO_2 were used as substrates. A multilayer MoS_2 material grown via metal–organic chemical vapor deposition (MOCVD) on sapphire developed by Grundmann *et al.* was used for this work.⁴³ The material was transferred onto the substrate via a wet transfer method with poly(methyl methacrylate) (PMMA) as a supporting layer. The PMMA/ MoS_2 layer was delaminated from the as-grown sapphire wafer via a 4 mol potassium hydroxide (KOH) solution and cleaned from the etchant by floating on DI water overnight. TOP-FETs and BOT-FETs were fabricated via optical lithography (EVG 420 Mask Aligner) with an AZ5214E resist (Merck Performance Materials GmbH). In the case of bottom-contact FETs (BOT-FETs), a 50 nm thick layer of Ni was initially sputter-treated via direct current (DC) sputtering via the von Ardenne sputter tool “CS 730 S” onto the substrate. After the lift-off process of the Ni layer in 80 °C acetone, MoS_2 was transferred onto the substrate, and subsequent patterning of the MoS_2 channel was achieved through reactive-ion etching (RIE) in an Oxford Instruments “Plasmalab System 100” tools with a mixture of tetrafluoromethane (CF_4) and oxygen gas. A reverse sputtering process was also achieved in the von Ardenne sputter tool in radio frequency (RF) mode, and the process pressure was 5×10^{-3} Torr. The reverse sputtering process was performed on the channel material of the devices to investigate the electrical properties. On the other hand, the fabrication of TOP-FETs started from the wet transfer of MoS_2 onto the substrate. Reverse sputtering was applied after the RIE process for channel patterning, followed by Ni deposition of the top electrodes. Note that only the MoS_2 at the contact regions of the TOP-

FETs was treated with reverse sputtering. In contrast, the MoS₂ in the channel region was protected by an AZ5214E photoresist during optical lithography, preserving its pristine state.

Material Characterization: Optical microscope images were recorded with a Leica INM100 microscope. Atomic force microscopy (AFM) measurements were performed on the as-grown MOCVD MoS₂ with an area of 5 μm × 10 μm on the sapphire wafer via Dimension Icon AFM by a Bruker instrument in tapping mode. Raman and PL measurements were conducted via an alpha300R WITec confocal Raman spectrometer with an excitation laser wavelength of 532 nm and a laser power of 1 mW. Measurements were performed in mapping mode at room temperature on an area of 5 × 5 μm with 2500 different points. The resolutions for PL and Raman were 300 g mm⁻¹ grating and 1800 g mm⁻¹ grating, respectively. The PL and Raman spectra were obtained by averaging the PL and Raman spectra measured at 2500 points. The film composition was analyzed via X-ray photoelectron spectroscopy (XPS) with a Thermo Scientific KA1066 spectrometer and monochromatic Al K-α X-rays at 1486.6 eV. To correct for potential charging effects in the XPS spectra, charge correction was applied to position the C-C bonding contribution from adventitious carbon at 284.8 eV. Contributions from O1s, S2p, Mo3d, and S1s (overlapping regions) were measured, and the atomic S to Mo ratios were calculated from the integrated peak areas via the appropriate sensitivity factors.

Electrical Measurements: The electrical characterization of the MoS₂-FETs consisted of measurements of the transfer and output characteristics. The measurements were performed in a cryogenic probe station “CRX-6.5K” from LakeShore Cryotronics connected to a Keithley

SCS4200 parameter analyzer. The probe station was conditioned either in vacuum (3×10^{-5} mBar) or under ambient conditions (42% humidity) in complete darkness and at room temperature (21 °C). Output curves were obtained by sweeping the V_{DS} from 0 V to 4 V at V_{GS} of 30 V to 40 V with an interval of 2 V, whereas transfer curves were obtained by sweeping the V_{GS} from -40 V to 40 V at a V_{DS} of 1 V.

Acknowledgments

This work has received funding from the European Union's Horizon 2020 and Horizon Europe Research and Innovation Programme under grant agreements Nos. 881603 (GrapheneCore3), 863258 (ORIGENAL), 952792 (2D-EPL), 101189797 (2D-PL) and 101135571 (AttoSwitch), from the German Federal Ministry of Education and Research, BMBF, within the projects NEUROTEC (Nos. 16ES1134 and 16ES1133K), NEUROTEC 2 (Nos. 16ME0399, 16ME0398K, and 16ME0400), and NeuroSys (No. 03ZU1106AA and 03ZU1106BA) and from the German Research Foundation (DFG) under grants LE 2440/7-1, LE 2440/8-1 and WA 4139/3-1 is gratefully acknowledged.

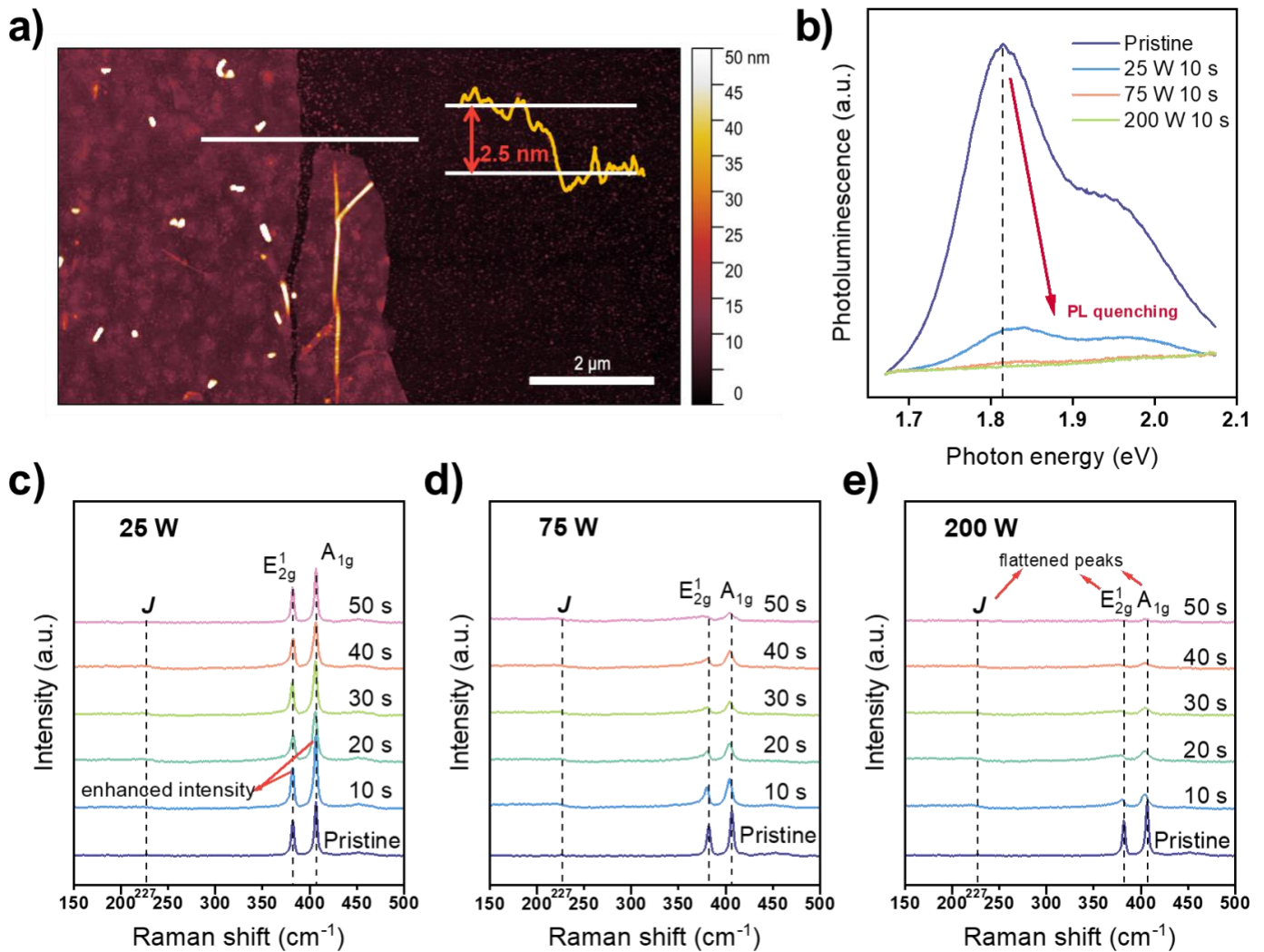


Figure 1: a) AFM image of MoS₂ on a SiO₂/Si substrate. The inset height profile shows a thickness of approximately 2.5 nm, indicating a multilayer MoS₂ film. b) PL spectra of pristine MoS₂ and MoS₂ under reverse sputtering at various powers and durations, showing a trend of PL quenching. Raman spectra of pristine 2D MoS₂ and sputter-treated MoS₂ at powers of c) 25 W, d) 75 W, and e) 200 W with increasing treatment duration until 50 s. The spectra of pristine MoS₂ in purple are located at the bottom of each series. The emerging *J* peak indicates distorted octahedral coordination of MoS₂, and the gradually flat spectra at 75 W and 200 W suggest that the crystal structure of MoS₂ is gradually destroyed.

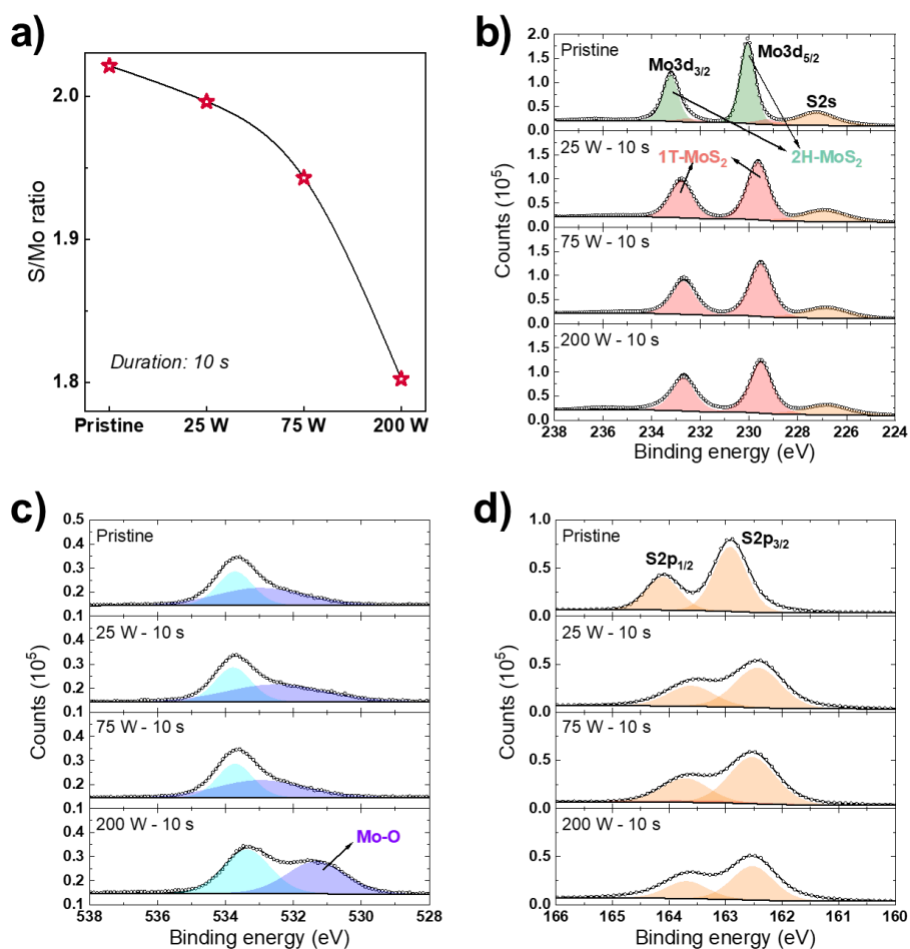


Figure 2: a) Sulfur to molybdenum ratio of the MoS₂ films as determined by XPS. The stoichiometry was calculated from the integrated peak areas of the Mo3d and S2p peaks. XPS spectra of b) Mo3d, c) S2p, and d) O1s. Note that there is an overlap with the S2s peak at a binding energy of approximately 227 eV. The spectra were fitted with three contributions for Mo3d. Two contributions corresponding to the 2H and 1T phases were fitted for the Mo3d⁴⁺ state. For these two Mo3d⁴⁺ contributions, the 1T phase contribution was constrained to have a 0.9 eV higher binding energy than the 2H contribution.³⁸ Upon sputtering, the O1s contribution at a lower binding energy increases.

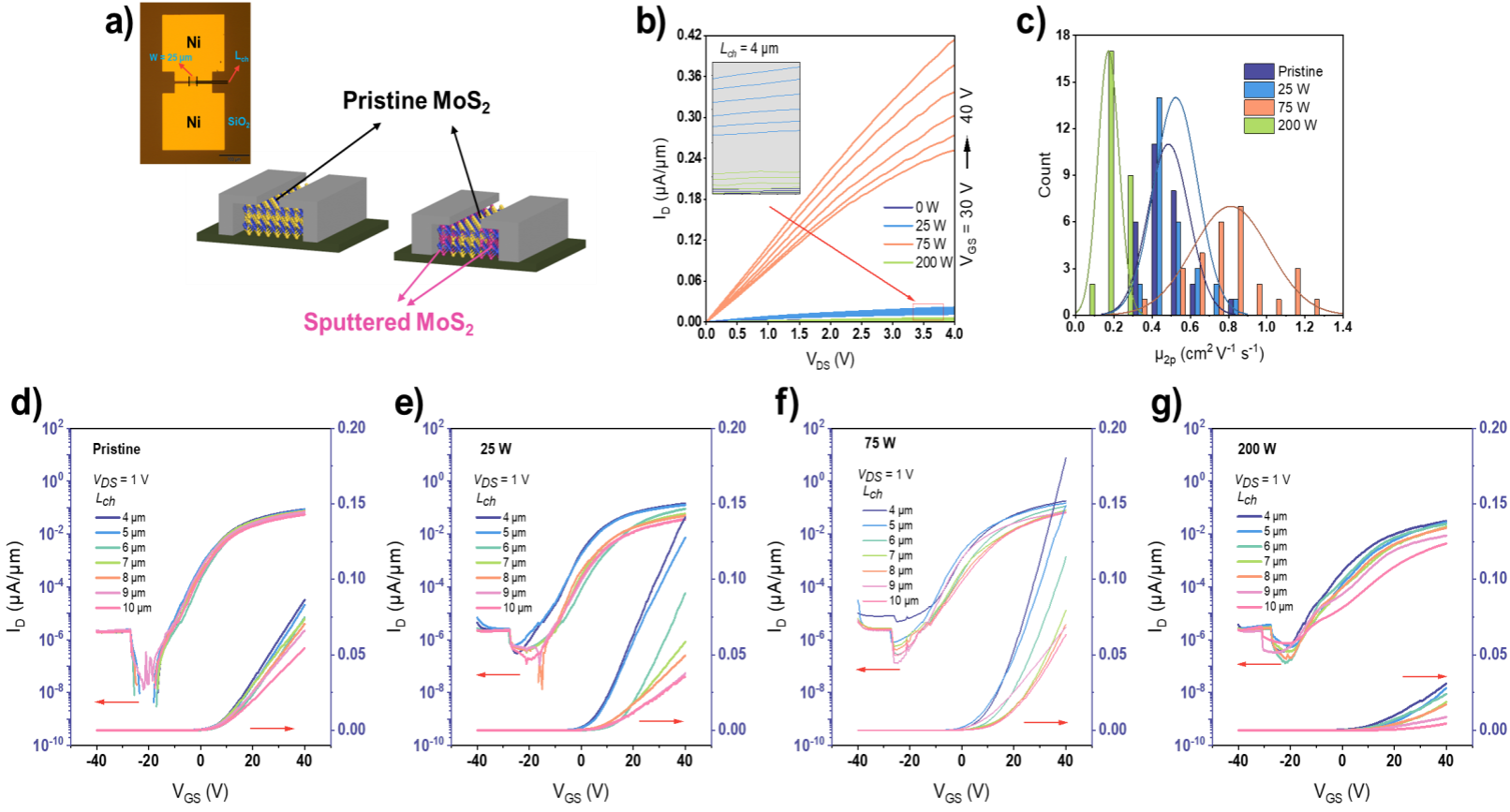


Figure 3: a) Schematics of a pristine MoS₂-FET (left) and a FET with a pristine MoS₂ channel combined with sputter-treated MoS₂ under the Ni electrodes (right). Inset: microscope image of a Ni-contacted MoS₂-FET. b) Output characteristics of TOP-FETs with $L_{ch} = 4 \mu\text{m}$ on the pristine sample (labeled 0 W) and samples under reverse sputtering of 25 W, 75 W, and 200 W. Inset: magnified view of the I_D of the pristine sample and samples treated with 25 W and 200 W sputtering power. c) Histogram of μ_{2p} of 28 TOP-FETs on each sample. The mean value and standard deviation are extracted by fitting a Gaussian distribution to the histogram data, where 75 W shows an enhanced μ_{2p} . d)-g) Transfer characteristics of pristine TOP-FETs and sputter-treated TOP-FETs at e) 25 W, f) 75 W, and g) 200 W in linear and logarithmic scales.

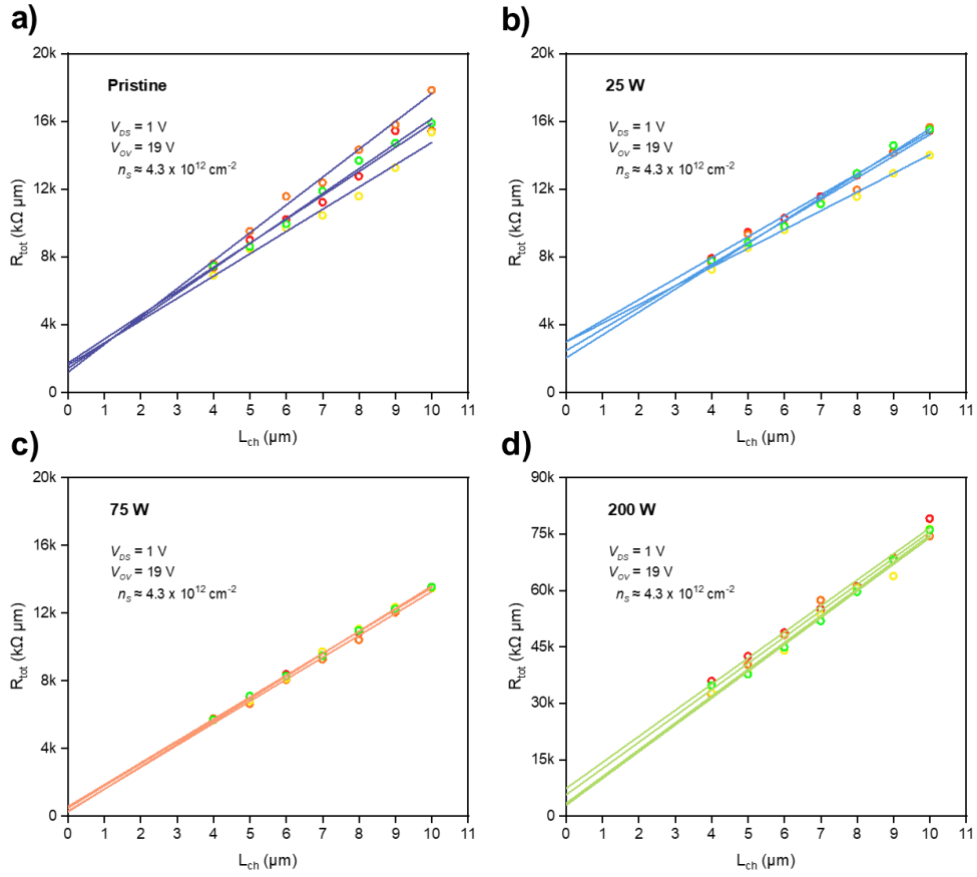


Figure 4: TLM plots of 4 groups of 7 TOP-FETs with L_{ch} ranging from 4 to 10 μm on a) the pristine sample, b) 25 W, c) 75 W, and d) 200 W samples with the same V_{OV} of 19 V.

Table 1: Mean R_c and R_{sh} with standard errors calculated via the TLM.

Sample	R_c ($\text{k}\Omega \cdot \mu\text{m}$)	R_{sh} ($\text{k}\Omega/\text{sq}$)
Pristine	1126 ± 1053	3058 ± 289
25 W	2632 ± 412	2484 ± 113
75 W	413 ± 167	2613 ± 146
200 W	4883 ± 2377	14081 ± 653

Reference

- (1) Akinwande, D.; Huyghebaert, C.; Wang, C.-H.; Serna, M. I.; Goossens, S.; Li, L.-J.; Wong, H.-S. P.; Koppens, F. H. L. Graphene and Two-Dimensional Materials for Silicon Technology. *Nature* **2019**, *573* (7775), 507–518. <https://doi.org/10.1038/s41586-019-1573-9>.
- (2) O'Brien, K. P.; Naylor, C. H.; Dorow, C.; Maxey, K.; Penumatcha, A. V.; Vyatskikh, A.; Zhong, T.; Kitamura, A.; Lee, S.; Rogan, C.; Mortelmans, W.; Kavrik, M. S.; Steinhardt, R.; Buragohain, P.; Dutta, S.; Tronic, T.; Clendenning, S.; Fischer, P.; Putna, E. S.; Radosavljevic, M.; Metz, M.; Avci, U. Process Integration and Future Outlook of 2D Transistors. *Nat. Commun.* **2023**, *14* (1), 6400. <https://doi.org/10.1038/s41467-023-41779-5>.
- (3) Lembke, D.; Bertolazzi, S.; Kis, A. Single-Layer MoS₂ Electronics. *Acc. Chem. Res.* **2015**, *48* (1), 100–110. <https://doi.org/10.1021/ar500274q>.
- (4) Kappera, R.; Voiry, D.; Yalcin, S. E.; Branch, B.; Gupta, G.; Mohite, A. D.; Chhowalla, M. Phase-Engineered Low-Resistance Contacts for Ultrathin MoS₂ Transistors. *Nat. Mater.* **2014**, *13* (12), 1128–1134. <https://doi.org/10.1038/nmat4080>.
- (5) Gan, X.; Lee, L. Y. S.; Wong, K.; Lo, T. W.; Ho, K. H.; Lei, D. Y.; Zhao, H. 2H/1T Phase Transition of Multilayer MoS₂ by Electrochemical Incorporation of S Vacancies. *ACS Appl. Energy Mater.* **2018**, *1* (9), 4754–4765. <https://doi.org/10.1021/acsaem.8b00875>.
- (6) Schneider, D. S.; Lucchesi, L.; Reato, E.; Wang, Z.; Piacentini, A.; Bolten, J.; Marian, D.; Marin, E. G.; Radenovic, A.; Wang, Z.; Fiori, G.; Kis, A.; Iannaccone, G.; Neumaier, D.; Lemme, M. C. CVD Graphene Contacts for Lateral Heterostructure MoS₂ Field Effect Transistors. *Npj 2D Mater. Appl.* **2024**, *8* (1), 35. <https://doi.org/10.1038/s41699-024-00471-y>.
- (7) Zhu, J.; Wang, Z.; Yu, H.; Li, N.; Zhang, J.; Meng, J.; Liao, M.; Zhao, J.; Lu, X.; Du, L.; Yang, R.; Shi, D.; Jiang, Y.; Zhang, G. Argon Plasma Induced Phase Transition in Monolayer MoS₂. *J. Am. Chem. Soc.* **2017**, *139* (30), 10216–10219. <https://doi.org/10.1021/jacs.7b05765>.
- (8) Xiao, J.; Chen, K.; Zhang, X.; Liu, X.; Yu, H.; Gao, L.; Hong, M.; Gu, L.; Zhang, Z.; Zhang, Y. Approaching Ohmic Contacts for Ideal Monolayer MoS₂ Transistors Through Sulfur-Vacancy Engineering. *Small Methods* **2023**, 2300611. <https://doi.org/10.1002/smt.202300611>.
- (9) Yoon, Y.; Ganapathi, K.; Salahuddin, S. How Good Can Monolayer MoS₂ Transistors Be? *Nano Lett.* **2011**, *11* (9), 3768–3773. <https://doi.org/10.1021/nl2018178>.
- (10) Piacentini, A.; Marian, D.; Schneider, D. S.; González Marín, E.; Wang, Z.; Otto, M.; Canto, B.; Radenovic, A.; Kis, A.; Fiori, G.; Lemme, M. C.; Neumaier, D. Stable Al₂O₃ Encapsulation of MoS₂-FETs Enabled by CVD Grown h-BN. *Adv. Electron. Mater.* **2022**, *8* (9), 2200123. <https://doi.org/10.1002/aelm.202200123>.
- (11) Radisavljevic, B.; Radenovic, A.; Brivio, J.; Giacometti, V.; Kis, A. Single-Layer MoS₂ Transistors. *Nat. Nanotechnol.* **2011**, *6* (3), 147–150. <https://doi.org/10.1038/nnano.2010.279>.
- (12) Valasa, S.; Tayal, S.; Thoutam, L. R.; Ajayan, J.; Bhattacharya, S. A Critical Review on Performance, Reliability, and Fabrication Challenges in Nanosheet FET for Future

- Analog/Digital IC Applications. *Micro Nanostructures* **2022**, *170*, 207374.
<https://doi.org/10.1016/j.micrna.2022.207374>.
- (13) Kumari, N. A.; Sreenivasulu, V. B.; Vijayvargiya, V.; Upadhyay, A. K.; Ajayan, J.; Uma, M. Performance Comparison of Nanosheet FET, CombFET, and TreeFET: Device and Circuit Perspective. *IEEE Access* **2024**, *12*, 9563–9571.
<https://doi.org/10.1109/ACCESS.2024.3352642>.
- (14) Uchida, K.; Koga, J.; Takagi, S. Experimental Study on Carrier Transport Mechanisms in Double- and Single-Gate Ultrathin-Body MOSFETs - Coulomb Scattering, Volume Inversion, and Δ /Sub SOI-Induced Scattering. In *Electron Devices Meeting, 2003. IEDM '03 Technical Digest. IEEE International*; 2003; p 33.5.1-33.5.4.
<https://doi.org/10.1109/IEDM.2003.1269402>.
- (15) Schmidt, M.; Lemme, M. C.; Gottlob, H. D. B.; Driussi, F.; Selmi, L.; Kurz, H. Mobility Extraction in SOI MOSFETs with Sub 1 Nm Body Thickness. *Solid-State Electron.* **2009**, *53*, 1246–1251. <https://doi.org/10.1016/j.sse.2009.09.017>.
- (16) Ellis, J. K.; Lucero, M. J.; Scuseria, G. E. The Indirect to Direct Band Gap Transition in Multilayered MoS₂ as Predicted by Screened Hybrid Density Functional Theory. *Appl. Phys. Lett.* **2011**, *99* (26), 261908. <https://doi.org/10.1063/1.3672219>.
- (17) Wang, L.; Liu, X.; Luo, J.; Duan, X.; Crittenden, J.; Liu, C.; Zhang, S.; Pei, Y.; Zeng, Y.; Duan, X. Self-Optimization of the Active Site of Molybdenum Disulfide by an Irreversible Phase Transition during Photocatalytic Hydrogen Evolution. *Angew. Chem.* **2017**, *129* (26), 7718–7722. <https://doi.org/10.1002/ange.201703066>.
- (18) Gao, G.; Jiao, Y.; Ma, F.; Jiao, Y.; Waclawik, E.; Du, A. Charge Mediated Semiconducting-to-Metallic Phase Transition in Molybdenum Disulfide Monolayer and Hydrogen Evolution Reaction in New 1T' Phase. *J. Phys. Chem. C* **2015**, *119* (23), 13124–13128.
<https://doi.org/10.1021/acs.jpcc.5b04658>.
- (19) Lin, Y.-C.; Dumcenco, D. O.; Huang, Y.-S.; Suenaga, K. Atomic Mechanism of the Semiconducting-to-Metallic Phase Transition in Single-Layered MoS₂. *Nat. Nanotechnol.* **2014**, *9* (5), 391–396. <https://doi.org/10.1038/nnano.2014.64>.
- (20) Piacentini, A.; Daus, A.; Wang, Z.; Lemme, M. C.; Neumaier, D. Potential of Transition Metal Dichalcogenide Transistors for Flexible Electronics Applications. *Adv. Electron. Mater.* **2023**, *9* (8), 2300181. <https://doi.org/10.1002/aelm.202300181>.
- (21) Prakash, A.; Ilatikhameneh, H.; Wu, P.; Appenzeller, J. Understanding Contact Gating in Schottky Barrier Transistors from 2D Channels. *Sci. Rep.* **2017**, *7* (1), 12596.
<https://doi.org/10.1038/s41598-017-12816-3>.
- (22) Schwarz, M.; Vethaak, T. D.; Derycke, V.; Francheteau, A.; Iniguez, B.; Kataria, S.; Kloes, A.; Lefloch, F.; Lemme, M.; Snyder, J. P.; Weber, W. M.; Calvet, L. E. The Schottky Barrier Transistor in Emerging Electronic Devices. *Nanotechnology* **2023**, *34* (35), 352002.
<https://doi.org/10.1088/1361-6528/acd05f>.
- (23) Shen, P.-C.; Su, C.; Lin, Y.; Chou, A.-S.; Cheng, C.-C.; Park, J.-H.; Chiu, M.-H.; Lu, A.-Y.; Tang, H.-L.; Tavakoli, M. M.; Pitner, G.; Ji, X.; Cai, Z.; Mao, N.; Wang, J.; Tung, V.; Li, J.; Bokor, J.; Zettl, A.; Wu, C.-I.; Palacios, T.; Li, L.-J.; Kong, J. Ultralow Contact Resistance between

- Semimetal and Monolayer Semiconductors. *Nature* **2021**, 593 (7858), 211–217.
<https://doi.org/10.1038/s41586-021-03472-9>.
- (24) Li, W.; Gong, X.; Yu, Z.; Ma, L.; Sun, W.; Gao, S.; Köroğlu, Ç.; Wang, W.; Liu, L.; Li, T.; Ning, H.; Fan, D.; Xu, Y.; Tu, X.; Xu, T.; Sun, L.; Wang, W.; Lu, J.; Ni, Z.; Li, J.; Duan, X.; Wang, P.; Nie, Y.; Qiu, H.; Shi, Y.; Pop, E.; Wang, J.; Wang, X. Approaching the Quantum Limit in Two-Dimensional Semiconductor Contacts. *Nature* **2023**, 613 (7943), 274–279.
<https://doi.org/10.1038/s41586-022-05431-4>.
- (25) Mondal, A.; Biswas, C.; Park, S.; Cha, W.; Kang, S.-H.; Yoon, M.; Choi, S. H.; Kim, K. K.; Lee, Y. H. Low Ohmic Contact Resistance and High on/off Ratio in Transition Metal Dichalcogenides Field-Effect Transistors via Residue-Free Transfer. *Nat. Nanotechnol.* **2024**, 19 (1), 34–43. <https://doi.org/10.1038/s41565-023-01497-x>.
- (26) Sun, Z.; Kim, S. Y.; Cai, J.; Shen, J.; Lan, H.-Y.; Tan, Y.; Wang, X.; Shen, C.; Wang, H.; Chen, Z.; Wallace, R. M.; Appenzeller, J. Low Contact Resistance on Monolayer MoS₂ Field-Effect Transistors Achieved by CMOS-Compatible Metal Contacts. *ACS Nano* **2024**, 18 (33), 22444–22453. <https://doi.org/10.1021/acsnano.4c07267>.
- (27) Mootheri, V.; Arutchelvan, G.; Banerjee, S.; Sutar, S.; Leonhardt, A.; Boulon, M.-E.; Huyghebaert, C.; Houssa, M.; Asselberghs, I.; Radu, I.; Heyns, M.; Lin, D. Graphene Based Van Der Waals Contacts on MoS₂ Field Effect Transistors. *2D Mater.* **2021**, 8 (1), 015003.
<https://doi.org/10.1088/2053-1583/abb959>.
- (28) Frindt, R. F. Single Crystals of MoS₂ Several Molecular Layers Thick. *J. Appl. Phys.* **1966**, 37 (4), 1928–1929. <https://doi.org/10.1063/1.1708627>.
- (29) McDonnell, S. J.; Wallace, R. M. Atomically-Thin Layered Films for Device Applications Based upon 2D TMDC Materials. *Thin Solid Films* **2016**, 616, 482–501.
<https://doi.org/10.1016/j.tsf.2016.08.068>.
- (30) Kang, N.; Paudel, H. P.; Leuenberger, M. N.; Tetard, L.; Khondaker, S. I. Photoluminescence Quenching in Single-Layer MoS₂ via Oxygen Plasma Treatment. *J. Phys. Chem. C* **2014**, 118 (36), 21258–21263. <https://doi.org/10.1021/jp506964m>.
- (31) Eda, G.; Yamaguchi, H.; Voiry, D.; Fujita, T.; Chen, M.; Chhowalla, M. Photoluminescence from Chemically Exfoliated MoS₂. *Nano Lett.* **2011**, 11 (12), 5111–5116.
<https://doi.org/10.1021/nl201874w>.
- (32) Nayak, A. P.; Pandey, T.; Voiry, D.; Liu, J.; Moran, S. T.; Sharma, A.; Tan, C.; Chen, C.-H.; Li, L.-J.; Chhowalla, M.; Lin, J.-F.; Singh, A. K.; Akinwande, D. Pressure-Dependent Optical and Vibrational Properties of Monolayer Molybdenum Disulfide. *Nano Lett.* **2015**, 15 (1), 346–353. <https://doi.org/10.1021/nl5036397>.
- (33) Livneh, T.; Sterer, E. Resonant Raman Scattering at Exciton States Tuned by Pressure and Temperature in 2 H -MoS₂. *Phys. Rev. B* **2010**, 81 (19), 195209.
<https://doi.org/10.1103/PhysRevB.81.195209>.
- (34) Li, H.; Zhang, Q.; Yap, C. C. R.; Tay, B. K.; Edwin, T. H. T.; Olivier, A.; Baillargeat, D. From Bulk to Monolayer MoS₂: Evolution of Raman Scattering. *Adv. Funct. Mater.* **2012**, 22 (7), 1385–1390. <https://doi.org/10.1002/adfm.201102111>.

- (35) Najmaei, S.; Liu, Z.; Ajayan, P. M.; Lou, J. Thermal Effects on the Characteristic Raman Spectrum of Molybdenum Disulfide (MoS₂) of Varying Thicknesses. *Appl. Phys. Lett.* **2012**, *100* (1), 013106. <https://doi.org/10.1063/1.3673907>.
- (36) Li, H.; Tsai, C.; Koh, A. L.; Cai, L.; Contryman, A. W.; Fragapane, A. H.; Zhao, J.; Han, H. S.; Manoharan, H. C.; Abild-Pedersen, F.; Nørskov, J. K.; Zheng, X. Activating and Optimizing MoS₂ Basal Planes for Hydrogen Evolution through the Formation of Strained Sulphur Vacancies. *Nat. Mater.* **2016**, *15* (1), 48–53. <https://doi.org/10.1038/nmat4465>.
- (37) Dieterle, M.; Mestl, G. Raman Spectroscopy of Molybdenum Oxides. *Phys. Chem. Chem. Phys.* **2002**, *4* (5), 822–826. <https://doi.org/10.1039/b107046k>.
- (38) Lin, Z.; Liu, Y.; Halim, U.; Ding, M.; Liu, Y.; Wang, Y.; Jia, C.; Chen, P.; Duan, X.; Wang, C.; Song, F.; Li, M.; Wan, C.; Huang, Y.; Duan, X. Solution-Processable 2D Semiconductors for High-Performance Large-Area Electronics. *Nature* **2018**, *562* (7726), 254–258. <https://doi.org/10.1038/s41586-018-0574-4>.
- (39) English, C. D.; Shine, G.; Dorgan, V. E.; Saraswat, K. C.; Pop, E. Improved Contacts to MoS₂ Transistors by Ultra-High Vacuum Metal Deposition. *Nano Lett.* **2016**, *16* (6), 3824–3830. <https://doi.org/10.1021/acs.nanolett.6b01309>.
- (40) Li, Y.; Wang, Y.; Lin, J.; Shi, Y.; Zhu, K.; Xing, Y.; Li, X.; Jia, Y.; Zhang, X. Solution-Plasma-Induced Oxygen Vacancy Enhances MoO_x/Pt Electrocatalytic Counter Electrode for Bifacial Dye-Sensitized Solar Cells. *Front. Energy Res.* **2022**, *10*, 924515. <https://doi.org/10.3389/fenrg.2022.924515>.
- (41) Nazir, G.; Khan, M. F.; Iermolenko, V. M.; Eom, J. Two- and Four-Probe Field-Effect and Hall Mobilities in Transition Metal Dichalcogenide Field-Effect Transistors. *RSC Adv.* **2016**, *6* (65), 60787–60793. <https://doi.org/10.1039/C6RA14638D>.
- (42) Islam, M. R.; Kang, N.; Bhanu, U.; Paudel, H. P.; Erementchouk, M.; Tetard, L.; Leuenberger, M. N.; Khondaker, S. I. Tuning the Electrical Property *via* Defect Engineering of Single Layer MoS₂ by Oxygen Plasma. *Nanoscale* **2014**, *6* (17), 10033–10039. <https://doi.org/10.1039/C4NR02142H>.
- (43) Grundmann, A.; McAleese, C.; Conran, B. R.; Pakes, A.; Andrzejewski, D.; Kümmell, T.; Bacher, G.; Teo, K. B. K.; Heuken, M.; Kalisch, H.; Vescan, A. MOVPE of Large-Scale MoS₂/WS₂, WS₂/MoS₂, WS₂/Graphene and MoS₂/Graphene 2D-2D Heterostructures for Optoelectronic Applications. *MRS Adv.* **2020**, *5* (31–32), 1625–1633. <https://doi.org/10.1557/adv.2020.104>.

Supporting Information

Contact Resistance Optimization in MoS₂ Field-Effect Transistors through Reverse Sputtering-Induced Structural Modifications

Yuan Fa^{1,2}, Agata Piacentini^{1,2}, Bart Macco³, Holger Kalisch⁴, Michael Heuken^{4,5}, Andrei Vescan⁴, Zhenxing Wang^{1,*}, and Max C. Lemme^{1,2,*}

1 AMO GmbH, Advanced Microelectronic Center Aachen, Otto-Blumenthal-Str. 25, 52074 Aachen, Germany

2 Chair of Electronic Devices, RWTH Aachen University, Otto-Blumenthal-Str. 25, 52074 Aachen, Germany

3 Department of Applied Physics and Science Education, Eindhoven University of Technology, 5600 MB Eindhoven, The Netherlands

4 Compound Semiconductor Technology, RWTH Aachen University, 52074 Aachen, Germany

5 AIXTRON SE, 52134 Herzogenrath, Germany

Bottom-contacted Field-Effect Transistors (BOT-FETs)

BOT-FETs were fabricated as a control experiment, where the entire MoS₂ in the channel and contact regions was exposed to the sputter treatment. Electrical measurements were conducted on the BOT-FETs under ambient conditions to assess the electrical properties of the sputter-treated MoS₂ channels. The device schematic is displayed in Fig. S5a. The treatment and measurement sequence followed the protocol used during Raman spectroscopy. Reverse sputtering was applied incrementally in 10-second intervals up to 50 s at 25 W, followed by an additional treatment at 200 W for up to 30 s. In Fig. S5b, the R_{tot} , which includes the resistance of the two contact regions and the channel region, is plotted against the duration of reverse sputtering of 25 W for three BOT-FETs with L_{ch} of 8, 9, and 10 μm and a W of 25 μm . Most strikingly, the R_{tot} of the three BOT-FETs experienced an evident decrease after an initial increase of 10 s. Subsequent application of 200 W after 25 W triggered a decrease in R_{tot} and then stabilized at a specific resistive level. In addition, compared with the overall decrease in R_{tot} , an abnormal increase in R_{tot} may be attributed to the worse contact properties under reverse sputtering. After applying 200 W for 30 s, R_{tot} decreased by two orders of magnitude compared with that of pristine BOT-FETs. We can infer that the MoS₂ crystalline structure is more sensitive to the sputtering power than to the sputtering duration. Fig. S5c shows the transfer curves of the BOT-FET with an L_{ch} of 8 μm obtained via the same sputter treatment method as in Fig. S5b. The transfer curves for reverse sputtering at 75 W and 200 W are shown in Fig. S5d-e. The pristine BOT-FET exhibits gate modulation with an on/off ratio of 10^4 . However, the gate modulation is severely weakened after treatment at 25 W for 10 s. The remaining transfer curves appear flat, suggesting the loss of gate modulation. Compared with

the pristine sample, the I_D of the BOT-FETs treated by 200 W reverse sputtering increased by more than five orders of magnitude, revealing the metallic property of the sputter-treated MoS₂. We also observed that the I_D after 50 s of sputter treatment is slightly lower than after 40 s. This could be explained by the fact that the sputter-treated MoS₂ may be oxidized in the ambient environment during the measurement, which is in agreement with the XPS results.

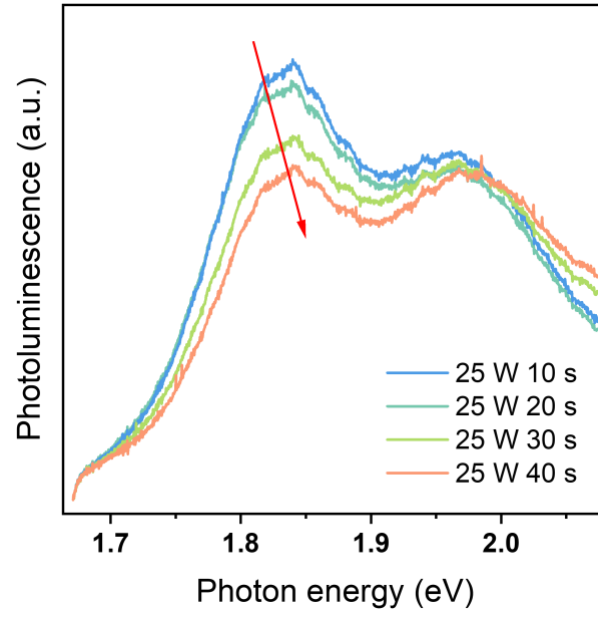


Figure S1: PL spectra at reverse sputtering at 25 W, showing gradually quenched PL peak as sputter duration increased.

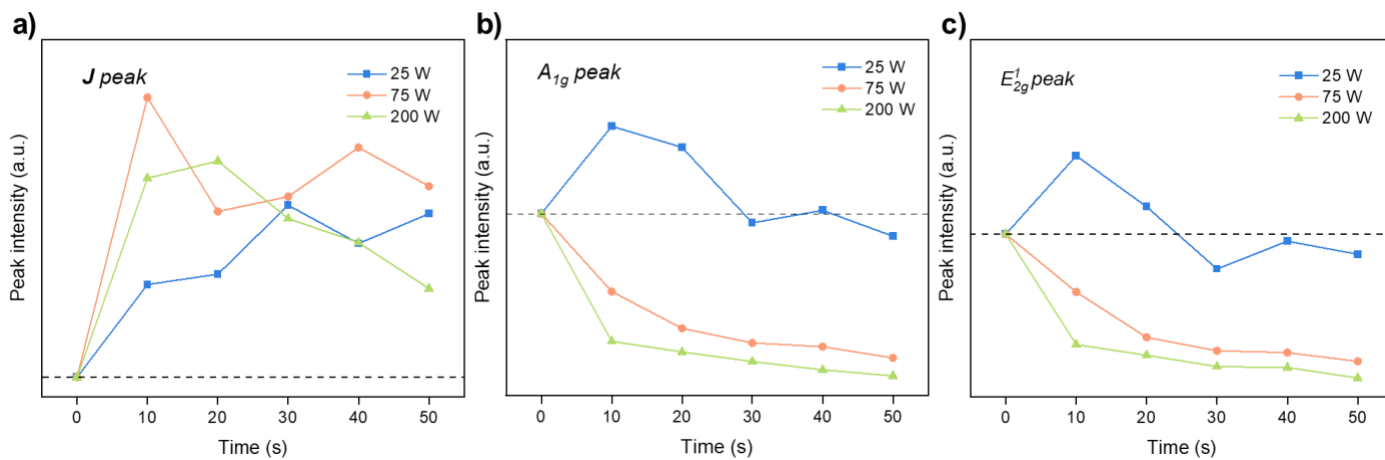


Figure S2: Changes in peak intensities of the a) J peak, b) A_{1g} peak, c) and E_{2g}^1 peak with increasing duration of reverse sputtering at 25 W, 75 W, and 200 W.

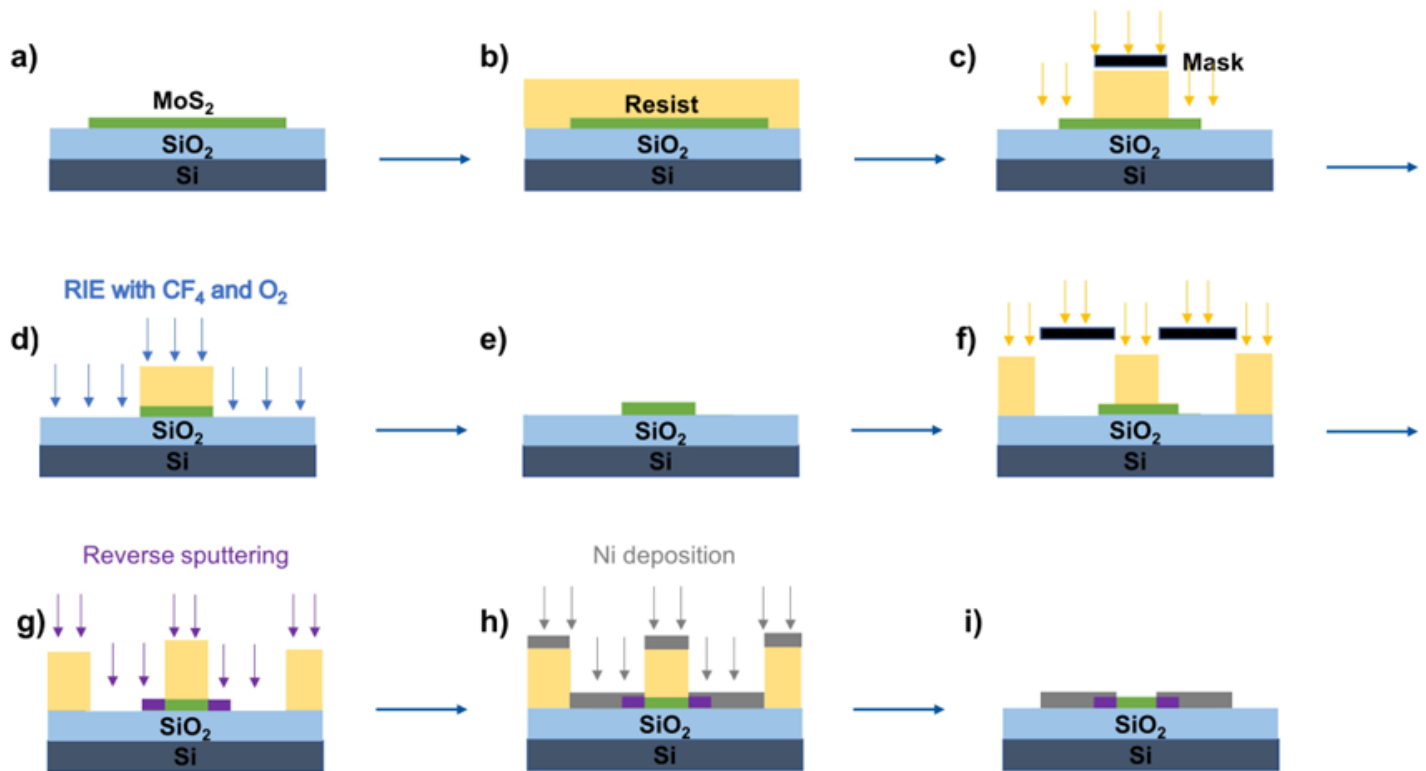


Figure S3: Schematic of the fabrication process of TOP-FETs with pristine channel MoS₂ and sputter-treated MoS₂ as contact electrodes: (a) wet transfer of 2D MoS₂ onto the SiO₂/Si substrate, (b) spin-coating of the AZ-5214E photoresist, (c) positive lithography, (d) RIE process, (e) image reversal lithography, (f) image reversal lithography, (g) reverse sputtering, (h) Ni sputtering process, and (i) cleaning of the resist and the final TOP-FETs.

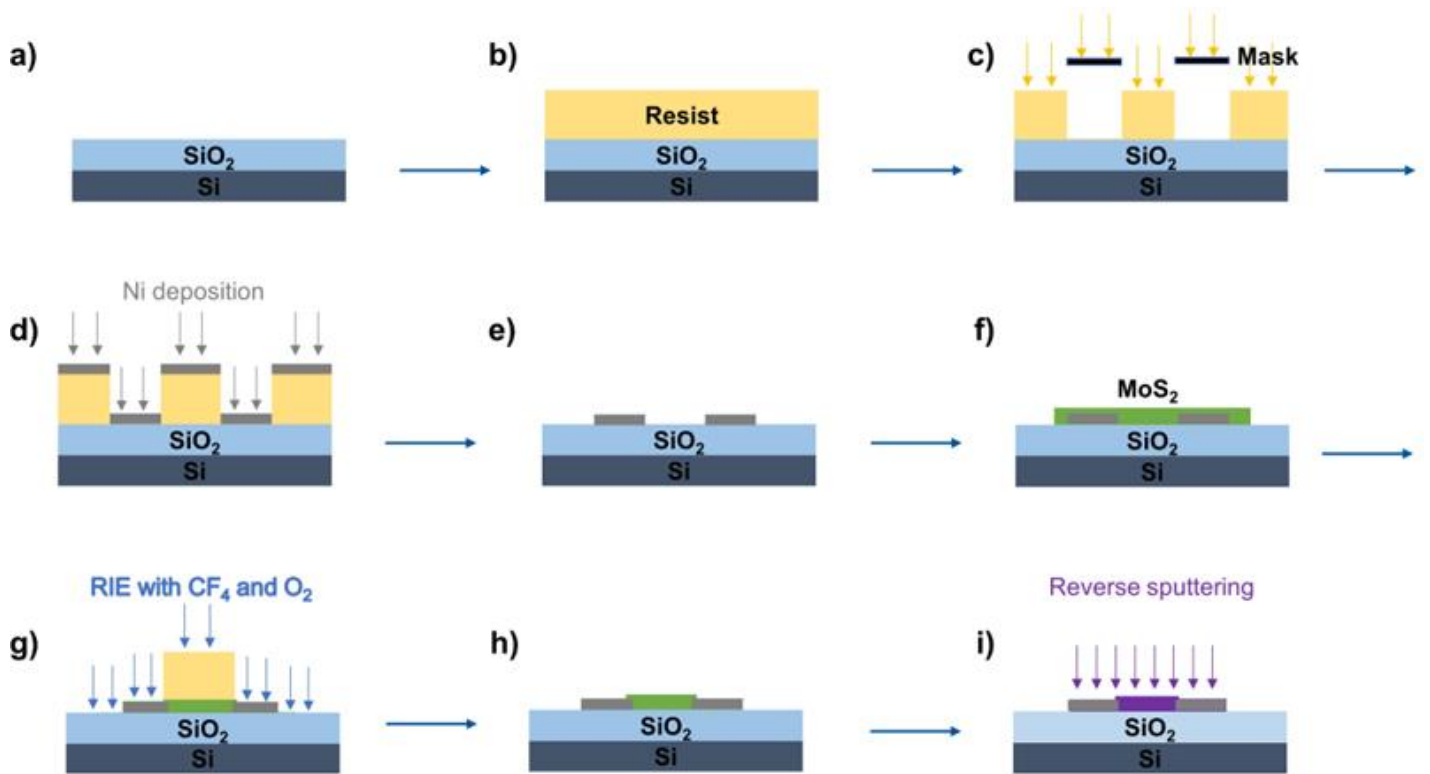


Figure S4: Schematic of the fabrication process of BOT-FETs with sputter-treated MoS₂: (a) Clean SiO₂/Si substrate, b) spin-coating of the AZ5214E resist, c) image reversal lithography, d) Ni sputtering process, e) lift-off process, f) wet transfer of 2D MoS₂ onto the metal pads, g) positive lithography and RIE process, h) cleaning of the photoresist, and i) reverse sputtering.

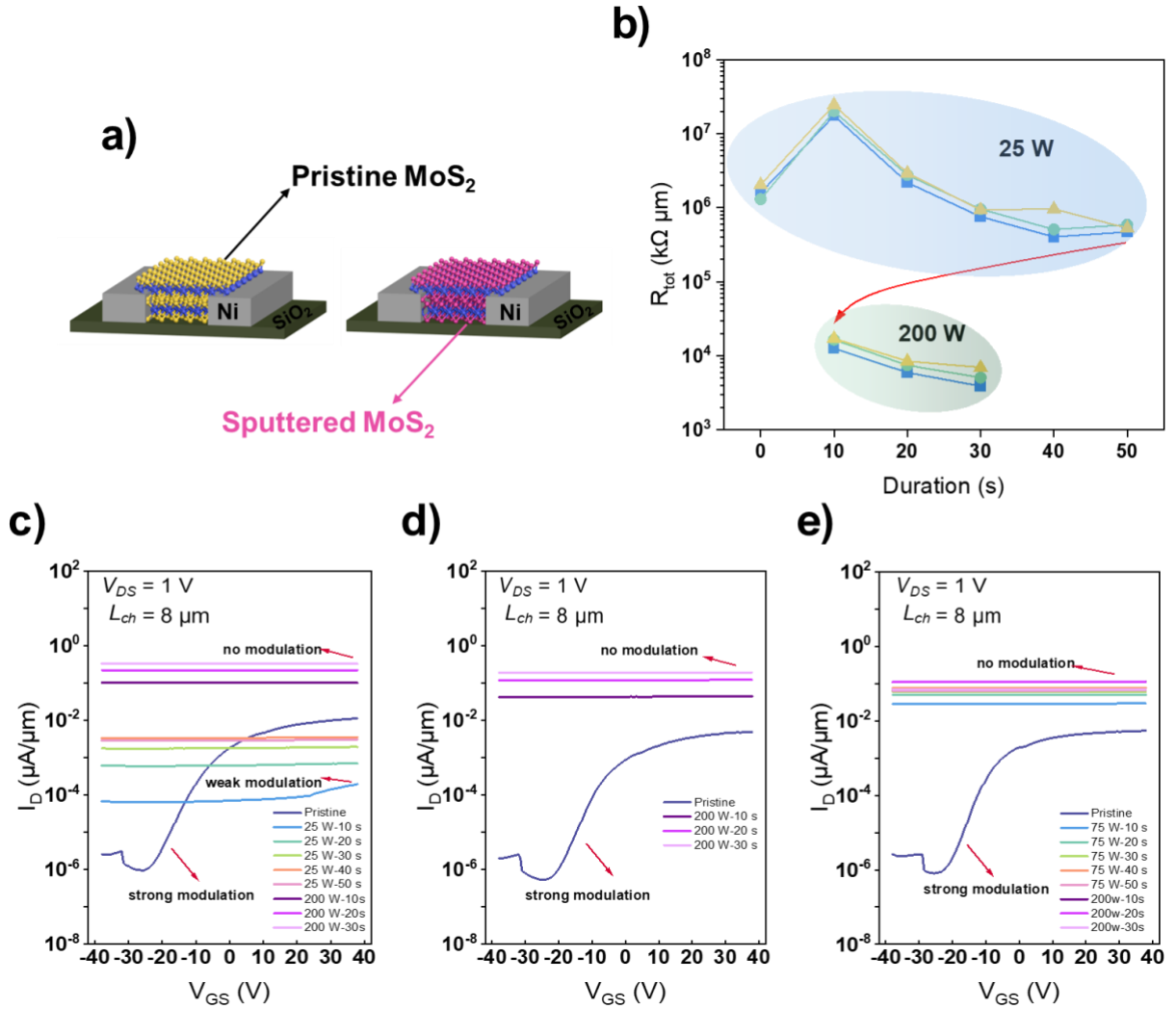


Figure S5: a) Schematics of the BOT-FETs. The MoS₂ in the right schematic is reverse sputter-treated with increasing treatment duration of up to 50 s. b) R_{tot} versus time with 25 W sputtering (up to 50 s) and 200 W sputtering, showing an abrupt change in R_{tot} and a weakened decreasing trend. c) Transfer curves of the BOT-FETs with the same treatment method as in b). The FET with pristine MoS₂ shows gate modulation, which is gradually lost after the FET is treated with reverse sputtering. The transfer curves of BOT-FETs subjected to reverse sputtering at d) 75 W and e) 200 W.